Università degli Studi di Padova

Dipartimento di Fisica e Astronomia "Galileo Galilei"

An improved simulation routine for modelling coherent high-energy proton interactions with bent crystals

Laurea Triennale in Fisica

Author:
Francesco Forcher

Supervisor:
Prof. Marco Zanetti

External Supervisors:
Dr. Daniele Mirarchi
Dr. Stefano Redaelli

Anno Accademico 2016/2017

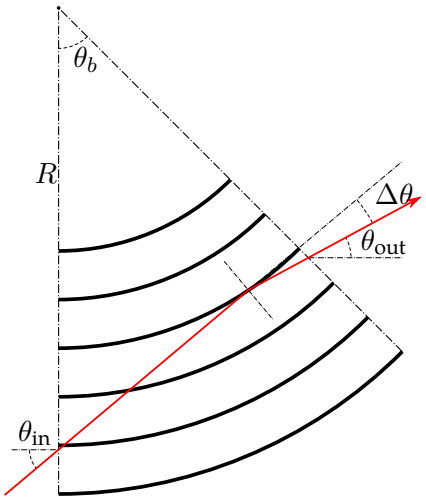

Volume reflection

Abstract

The planes in crystalline solids can constrain the directions that charged particles take as they pass through. Physicists can use this "channelling" property of crystals to steer particle beams. In a bent crystal, for example, channelled particles follow the bend and can change their direction. Experiments are being carried out to study in detail this phenomenon. The UA9 collaboration is using high energy protons and heavy ions beams from the SPS accelerator at CERN to verify the possibility of using bent crystals as primary collimators in high energy hadron colliders like the LHC. Simulations have been developed to model the coherent interaction with crystal planes. The goal of the thesis is indeed to analyze the data and develop an improved simulation routine to better describe the data's subtleties, in particular the transition between the volume capture and amorphous modes of beam interaction with the crystal.

CONTENTS

I Introduction and goals **1**

II Crystal collimation physics **2**
I Channeling . . . 3
II Bent crystals . . . 7
III Volume reflection . . . 8
IV Dechanneling and Volume Capture . . . 9

III Experimental apparatus **9**
I Measurement methods . . . 10

IV Data analysis **12**
I Error estimates with bootstrap . . . 14
II Theoretical model . . . 16

V Benchmark simulation results **19**
I Crystals used . . . 19
II Benchmark . . . 19
III Energy scaling . . . 23

VI Conclusions **24**

LIST OF FIGURES

1 Diamond cubic structure of Si . . . 2
2 System of reference . . . 2
3 Crystalline planes potential . . . 3
4 The harmonic approximation of the potential . . . 4
5 Particle system of reference with respect to crystalline planes 5
6 Bent planes potential in non-inertial reference frame . . . 7
7 Geometric characteristics of volume reflection . . . 9
8 Experimental apparatus . . . 9
9 Example of angular scan . . . 11
10 Experimental angular scan . . . 12
11 Old simulation . . . 13
12 Region slicing . . . 15
13 Slices examples . . . 15
14 Fitting results: weights . . . 16
15 Theoretical model weights . . . 17
16 Theoretical model means . . . 18

17 Simulated angular scan 18
18 Simulation: STF45 weights 20
19 Simulation: STF99 weights 21
20 Simulation: ST101 weights 21
21 Simulation: ST101 means 22
22 Simulation: ST101 sigmas 22
23 Loss map simulation comparison 23

I. INTRODUCTION AND GOALS

DURING THE SECOND HALF of the 20th century, various landmark experiments showed that the penetration distance of charged particles along specific directions in crystalline materials was much longer than expected from amorphous scattering theory.

The theory developed postulates that the particles, depending on the impact parameter, can interact with the ordered structure of the atoms in crystals. For example, one of the most interesting phenomena for practical applications is the *channeling* process, in which a beam of positive particles, which impact on the crystal with an angle almost parallel to the crystal planes, can be trapped in the potential well, forcing them to oscillate between such planes. If one then bends the crystal, the particles will be guided and steered by the crystalline planes, resulting in large net kicks, much larger than what can be achieved using magnetic fields.

Another phenomenon can happen when a particle beam interact with a crystal: a particle can be reflected by crystal planes, causing an angular deflection to the opposite direction of the atomic plane bending. This process is called *volume reflection*, and sparked some interest because it has a very high deflection efficiency, approaching 95% almost independently of particle energy or crystal curvature. For comparison, channeling has a single-pass efficiency of about 60%. Nevertheless, when in circular accelerators the beam passes multiple times through the crystal, scattering can bring a particle in the channeling conditions after a few turns, realizing a total efficiency af about 90%. This and the fact that volume reflection has a higher number of unwanted nuclear interactions, makes channeling still preferable in pratical accelerator applications.

The work of this thesis focuses on the modelization and simulation of the "transition region", that is, the angular range in which both volume reflection and amorphous scattering coexist.

After briefly reviewing in **Section II** the salient points of crystal physics, in **Section III** the experimental apparatus and instruments used for data taking are illustrated. In **Section IV** the details of the data selection and analysis are explored, and then in **Section V** the simulation results are compared to the experiments. Finally, in **Section VI** the results for this model are considered.

II. Crystal collimation physics

Beam collimation is a branch of accelerator physics concerned with the handling and disposal of particles lost from the beam, to protect the magnets and equipment.

The interest about crystals for collimation applications derives from their ability to precisely control some parameters of particle beams, by variating the relative angle of the crystal with respect to the particle beam. This is due to the fact that they have an ordered microscopic structure: atoms in a crystal are arranged in a regular symmetrical structure. As explained in this section, this leads to peculiar behaviours caused by this anisotropy.

Although many different kinds of crystalline materials have been tested for use in accelerators, currently the best candidates remain silicon crystals (shown in **Fig. 1**), for which, thanks to their application in semiconductor industry, advanced methods for reaching extreme levels of purity have been developed. From this follows that crystalline defect theory can be ignored and they can be considered perfect crystals, for the practical purposes of collimation.

In **Fig. 2** the system of reference of the crystal used hereafter is shown.

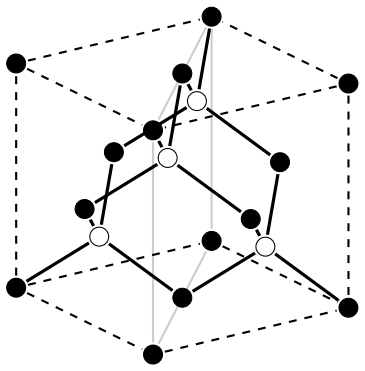

Figure 1: *The diamond cubic structure of monocrystalline silicon: it's a face-centered cubic lattice with two basis atoms. Evidenced by the grey cut the* (110) *plane.*

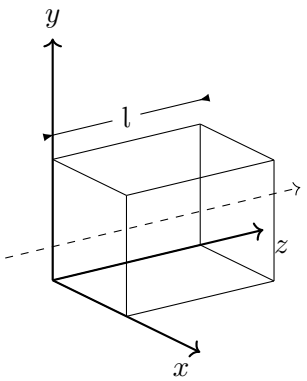

Figure 2: *The system of reference used. The parallelepiped represent the crystal and the dashed arrow show the direction of the beam, going along the z direction. The crystal has thickness l.*

II.I Channeling

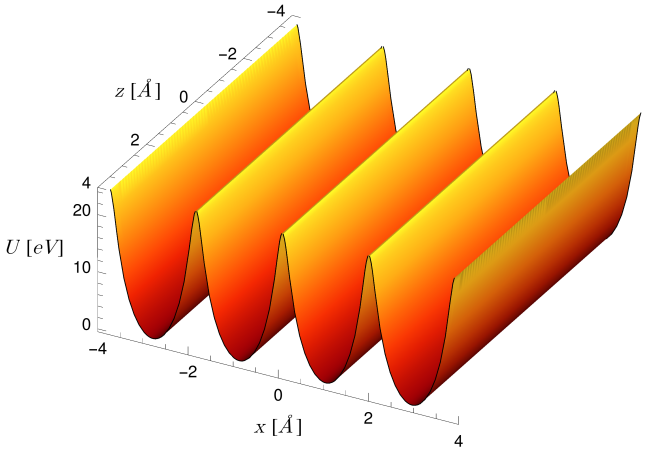

Figure 3: *Plot of the crystalline planes potential $U(x, z)$ of (110) silicon, along the X and Z coordinates, for a positive charge (otherwise the sign should be flipped) particle coming along the x direction.*

THE MOST IMPORTANT PHENOMENON for practical applications in beam collimation is the so-called *planar channeling*: a particle entering almost parallel to the crystalline planes could remain trapped in between them, moving in a relatively empty space thanks to the interplanar atomic potential which steers it away from nuclei, leaving only the weaker electron cloud interactions to obstaculate its path. In a straight crystal, this results in a much longer penetration depth of a particle beam for some specific orientations of the crystal, those where most of the beam enters the crystal "straight enough" relative to the planes.

If the particle enters with a small angle with respect to the planes, we can replace the potential from the single atoms with a continuous potential. This potential U_{pl} from a single plane [1] is obtained from integrating the Thomas-Fermi atomic charge distribution over the crystal planes.

$$U_{\text{pl}}(x) \approx N d_p \iint_{-\infty}^{\infty} \frac{Z_i Z e^2}{r} \Phi\left(\frac{r}{\alpha_{\text{TF}}}\right) \mathrm{d}x\mathrm{d}y \tag{1}$$

where Z_i and Z are the charge numbers of the incident particle and of the material nuclei respectively, d_p the interplanar spacing, e the elementary charge, N is the number of atoms per volume, $\alpha_{\text{TF}} = 0.8853 \cdot 0.529 Z^{-1/3}$Å is the Thomas-Fermi screening distance, and $\Phi(r)$ the screening function.

Then, since contribution from the two nearest planes dominate [1], it can be assumed that the particle is subject to the potential from the two

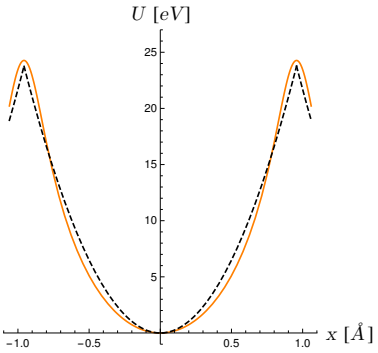

Figure 4: *The real potential between two planes (orange line) compared with the harmonic approximation fitted to it (dashed line).*

closest ones (defining $U(0) = 0$):

$$U(x) \approx U_{\text{pl}}\left(\frac{d_p}{2} - x\right) + U_{\text{pl}}\left(d_p/2 + x\right) - 2U_{\text{pl}}\left(\frac{d_p}{2}\right) \tag{2}$$

and, repeating this pattern for all the planes, the plot shown in **Fig. 3** is obtained. It is clear from **Fig. 4** that it can be approximated quite precisely by an harmonic potential [1]

$$U_h(x) = U_0\left(\frac{2x}{d_p}\right)^2 \quad \text{where} \quad U_0(\text{Si}) \approx 20\,\text{eV}. \tag{3}$$

Particles motion between crystalline planes can be treated with classical mechanics because the potential well depth of silicon planes is of the order of $20\,\text{eV}$, and it can be shown [1] that a particle in a channel oscillates as if having a relativistic mass $M\gamma$, so the total number N_l of energy levels inside the harmonic potential (3) of depth $U_0 = 20\,\text{eV}$ is

$$N_l = \frac{d_p}{\hbar\sqrt{8}}\sqrt{U_0 M\gamma}\,. \tag{4}$$

Classical mechanics is applicable if $N_l \gg 1$. This number is of the order of $4 \cdot 10^{13}$ for $400\ \text{GeV}/c$ proton beams used for the data in this thesis, so the energy states can be regarded as continuous and consider a classical approach.

To write the equations of motion of a particle trapped in a potential channel $U(x)$, it is convenient to consider the conservation of energy [1]:

$$E = \sqrt{p_t^2c^2 + p_l^2 + m^2c^4} + U(x) = \text{const} \tag{5}$$

where p_t is the transverse component of momentum and p_l the longitudinal one, as illustrated in **Fig. 5**.

Assuming that the angle θ is small (so that the particle enters almost parallel to the planes) it follows that

$$\theta \approx \tan(\theta) = {}^{p_t}/_{p_l} \ll 1 \quad \Longrightarrow \quad p_t \ll p_l \tag{6}$$

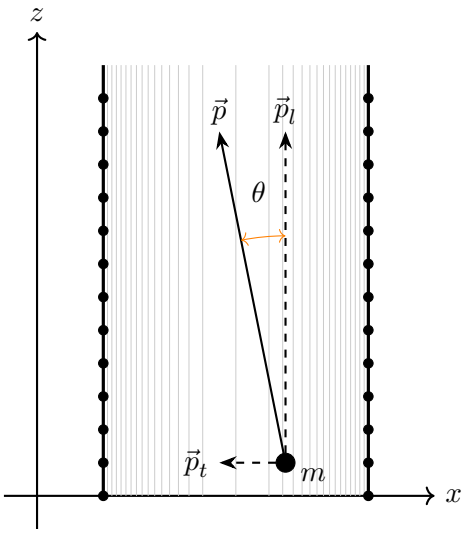

Figure 5: *Plot of a particle in a potential channel, viewed from above. The crystalline planes are represented by the bold lines and dots, while the light gray lines are the potential level curves* $L_c(U) = \{x, z \mid U(x, z) = c\}$. *The mass* m *particle has momentum* $\vec{p}$ *decomposed into the longitudinal and transverse components* $\vec{p}_l$ *and* $\vec{p}_t$*, while* θ *is the angle between* $\vec{p}$ *and the planes.*

so equation (5) can be approximated as

$$\frac{p_t^2 c^2}{2E_l} + U(x) + E_l = \text{const}, \quad \text{where} \quad E_l = \sqrt{p_l^2 + m^2 c^4}. \tag{7}$$

As it is shown in **Figure 5**, $\vec{p}_l$ is conserved since there are not any forces along the longitudinal direction, and so E_l is conserved as well. This implies that the sum of the first two terms in equation (7), called the *transverse energy* E_t, is conserved too:

$$E_t = \frac{p_t^2 c^2}{2E_l} + U(x) = \frac{p_l^2 c^2}{2E_l}\theta^2 + U(x) = \text{const} \tag{8}$$

using $p_l \approx p_t\theta$ from equation (6). From there also $E_l \approx E$ and $p_l \approx p$ can be inferred, and using the known relation $pc^2 = vE$ with v particle velocity, (8) can be rewritten to obtain:

$$E_t = \frac{pv}{2}\theta^2 + U(x) = \text{const} \tag{9}$$

The reduced one-dimensional system can now be solved in x and the position $x_p(z)$ of the particle is obtained, taking into account that $\theta(z) = \frac{dx_p(z)}{dz}$ and differentiating (9) with respect to z:

$$\begin{aligned} \frac{pv}{2}\theta\left(z\right)^2 + U\left(x_p(z)\right) &= E_t \\ pv\theta'(z)\theta(z) + U'\left(x_p(z)\right)x_p'(z) &= 0 \\ \theta(z)\left(pv\frac{d^2x_p}{dz^2} + U'\left(x_p\right)\right) &= 0 \end{aligned}$$

finally obtaining

$$pv\frac{d^2x_p}{dz^2} + U'\left(x_p\right) = 0\,. \tag{10}$$

This is the equation of motion of a channeled particle, and, substituting $U(x_p)$ with the the harmonic potential (3) introduced earlier, which leads to an harmonic oscillator equation

$$pv\frac{d^2x_p}{dz^2} + \frac{8U_0}{d_p^2} = 0\ . \tag{11}$$

This can be solved to get a sinusoidal motion

$$x_p(z) = \frac{d_p}{2}\sqrt{\frac{E_t}{U_0}}\sin\left(\frac{2\pi z}{\lambda} + \phi\right) \tag{12}$$

$$\theta(z) = \sqrt{\frac{2E_t}{pv}}\cos\left(\frac{2\pi z}{\lambda} + \phi\right) \tag{13}$$

with ϕ being the entry phase and

$$\lambda = \pi d_p\sqrt{\frac{pv}{2U_0}}\ . \tag{14}$$

being the oscillation period.

To get in channeling, the condition $E_t < U_0$ needs to be fulfilled, using equation (9) this can be rewritten as

$$E_t = \frac{pv}{2}\theta^2 + U(x) \leq U_0\ . \tag{15}$$

When $x = 0$ (remembering that by definition $U(0) = 0$) θ can be solved for to obtain the *critical channeling angle* (in a straight crystal)

$$\theta_c^0 = \sqrt{\frac{2U_0}{pv}} \tag{16}$$

which is the maximum angle for which the particle can get trapped between the crystal planes.

The importance of channeling has thus been shown, as the particles are coherently steered by the planes in a relatively empty space, so avoiding the "hard" nuclear strong interactions that produce undesired energy loss and secondary products. Also, as shown in the next section, crystals can be bended and (within certain limits) the particles will follow the crystal bending, thus opening the possibility to guide a particle beam towards a target, such as a massive absorber for example [4].

This theory implies as well that materials such as tungsten crystals could have better theoretical characteristics for collimation, because they have a $\sim$15 times stronger maximum atomic electric field [1]. Unfortunately at this moment their fabrication process leaves them with too many defects to be useful for collimation.

II.II Bent crystals

Bending slightly a crystal by a *bending angle* θ_b introduces an additional centrifugal force in the non-inertial reference frame [1], thus modifying equation (11) into

$$pv\frac{d^2x_p}{dz^2} + U'(x_p) + \frac{pv}{R} = 0\,. \tag{17}$$

where R is the curvature radius. Now an effective transverse energy can be written:

$$E_t = \frac{pv}{2}\theta^2 + U_{\text{eff}}(x) = \frac{pv}{2}\theta^2 + U(x) + \frac{pv}{R}x\,, \tag{18}$$

with an effective potential U_{eff}, plotted in **Fig. 6**.

Qualitatively, the trajectory of the particle is similar to the unbent one, a sinusoidal oscillation, but the equilibrium point is be shifted closer to the planes by centrifugal forces.

As shown, it is also clear that the effective potential well is reduced by curving the crystal, until it disappears completely at the *critical radius* $R_c(E)$, depending on particle energy, after which channeling is no longer possible. To consider the non-zero width of the atomic planes (which is about α_{TF}), the *critical radius* R_c is found [4] as the as the radius at which the centrifugal force is equal to the maximum electric force between the planes:

$$R_c = \frac{pv}{U'(x_c)} \approx \frac{pvx_{\text{max}}}{2U_{\text{max}}}\,. \tag{19}$$

The reduction in depth of the potential well affects the particles critical angle, which is reduced as [1]:

$$\theta_c(R_c/R) = \theta_c^0\,(1 - R_c/R)\ . \tag{20}$$

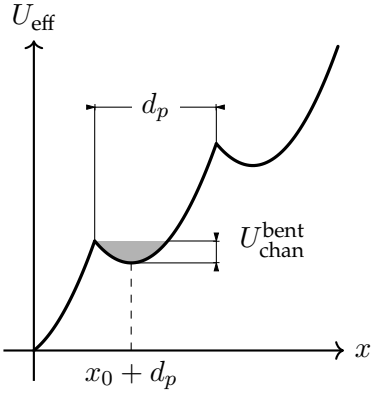

Figure 6: *Potential in the non-inertial reference frame in bent crystals. The new equilibrium point is at $x = x_0$ ($+d_p$ for these two particular planes). The grey area is the new effective channeling potential well of depth U_{chan}^{bent}, when $R > R_c$. The particles oscillate closer to the crystalline planes, increasing the possibility of nuclear interactions.*

So in conclusion, a particle channeled for the whole crystal length will be deflected by an angle of $\theta_b = {}^{l}/_{R}$, where l is the length of the crystal. The equation of motion solution can be written as [1]

$$x = -x_c \frac{R_c}{R} + x_c \sqrt{\frac{E_T}{U_{\text{chan}}^{\text{bent}}}} \sin\left(\frac{2\pi z}{\lambda} + \phi\right) \tag{21}$$

where $x_0 = -x_c \frac{R_c}{R}$ is the new equilibrium point and λ and ϕ the same as before.

II.III Volume reflection

IN BENT CRYSTALS another phenomenon [9] can take place when a particle does not have the right angle for channeling: if the incoming angle is greater (toward the bending direction) than the θ_c necessary for channeling but still smaller than θ_b, the particle may be "reflected off" the crystalline planes, as shown in **Fig. 7**.

As evident from the figure, from geometrical considerations alone the particle would not find a suitable plane if $\theta_{\text{in}} > \theta_b$, explaining the second condition. Nevertheless, as it will be explored in this thesis, it has been demonstrated experimentally that in a range between

$$\theta_b < \theta_{\text{in}} < \theta_b + 2\theta_c \tag{22}$$

coherent and incoherent interactions exist coexist together.

Volume reflection is interesting because it has a very high deflection efficiency, approaching 95% (against the average of 60% for channeling) [4], but suffers from a fivefold increase in nuclear interactions which generates a lot of unwanted off-momentum particles, and the $\Delta\theta$ that can be given by volume reflection is much lower than the one potentially given by channeling (of the order of θ_c rather than θ_b)

In fact, simulations and experiments [10][8] show that the *average deflection angle* $\Delta\theta = \theta_{\text{VR}}$ and its spread $\sigma_{\theta_{\text{VR}}}$ can be fitted as follows:

$$\theta_{\text{VR}} = c_1 \theta_c \left(1 - c_2 \frac{R_c}{R}\right) \tag{23}$$

$$\sigma_{\theta_{\text{VR}}} = c_3 \theta_c \frac{R_c}{R} \tag{24}$$

where $c_1 = -1.5$, $c_2 = 1.666$, and $c_3 = 1.7$. It is worth noticing how from these follows $\theta_{\text{VR}} \approx 1.6\theta_c$ when $R \gg R_c$.

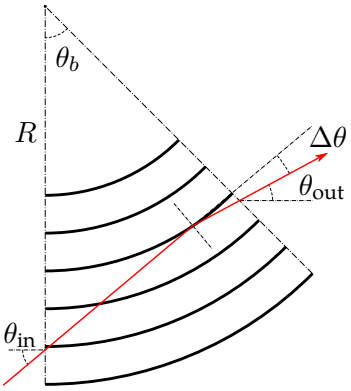

Figure 7: *The geometric characteristics of volume reflection. The crystal is bent by an angle θ_b, resulting in a curvature radius of R. The particle enters with an angle of θ_{in} until it impacts upon a tangent plane by which is reflected off, exiting the crystal with an angle of θ_{out}, giving a total deflection of $\Delta\theta$.*

II.IV Dechanneling and Volume Capture

Two other phenomenons, which are not addressed in the following work, can characterize the trajectory of a particle in a crystal: *dechanneling* and *volume capture*. Random collisions with electrons and atomic nuclei can change the transverse momentum of a particle: in the dechanneling case this leads a channeled particle to be kicked out of channeling and exit with an intermediate deflection of $0 < \theta < \theta_b$. Conversely, in the volume capture case a particle in the angular range of volume reflection falls in the potential well, and enters channeling mode.

III. EXPERIMENTAL APPARATUS

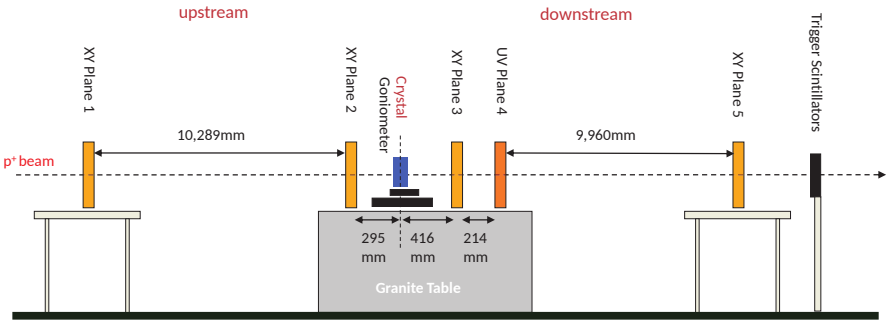

Figure 8: *Illustration (taken from [6]) showing the experimental apparatus setup. The beam enters from the left.*

THE EXPERIMENTAL APPARATUS (described in [6]) is shown in **Fig. 8**. It is installed in the H8 extraction line of the SPS accelerator, in the North Area of CERN. It consist of five tracking stations (labeled *XY Plane* in figure) which are made each by two planes of microstrip silicon

detector stations, with an active area of $3.8 \times 3.8\ \mathrm{cm}^2$. The particles first pass through station 1 and 2 which measure the entry angle θ_{in}, then they interact with a target station (typically a goniometer where the crystal is installed). After, stations 3 and 5 measure the exit angle θ_{out} (station 4, rotated 45°, is used to resolve ambiguities in multi-track events), and finally a plastic scintillator provides the trigger.

Vacuum chambers are placed between the stations 1 and 2 and between 4 and 5, so the main limiting factor to the telescope resolution is multiple coulomb scattering in the detectors.

The spatial linear resolution, used to select protons impacting on the crystals, has an average value of $\sim$7 $\mu\mathrm{m}$ [6]. The angular resolution of the incoming arm of the telescope is important for selecting particles impacting with a desired angle: since it cannot be disentagled from the intrinsic beam divergence in measurements, it is estimated using Monte-Carlo simulations of the apparatus, and the result is of about $\sim$2.8 $\mu\mathrm{rad}$ [6].

The angular resolution on the deflection ($\Delta\theta = \theta_{\text{out}} - \theta_{\text{in}}$) can be instead estimated experimentally. This measurement is performed by removing the crystal from the beam line. Thus particles follow a straight trajectory and $\theta_{\text{in}} = \theta_{\text{out}}$ is espected. This would be the case in an ideal apparatus with infinite resolution, however, given the multiple coulomb scattering in the tracking plane and uncertainties in the tracks reconstruction, a gaussian distribution is obtained when performing an histogram of $\Delta\theta$. The RMS of such gaussian gives the telescope resolution on the measured deflection.

III.I Measurement methods

For our purposes, four measurement steps are carried out to characterize each crystal [4]:

1. **Alignment run:** done without the crystal, to check proper functioning and performance of the telescope.

2. **Linear scan:** the crystal is moved linearly to correctly position it on the beam line. The increased beam divergence due to multiple coulomb scattering shows where the crystal is.

3. **Fast angular scan:** the crystal is rotated around to identify the angular ranges where coherent interactions take place.

4. **Detailed angular scan:** this angular scan is performed around the interesting angular range determined in the step before, collecting a consistent number of events ($\sim 10^5$ events / step)

The most useful type of scan for the analyses made in this thesis is the detailed angular scan: an example is shown in **Fig. 9**. From this figure it is possible to see all the different processes that can take place in bent crystals:

1. **Amorphous:** the particle does not interact coherently with the crystal planes, so the average deflection $\Delta\theta_x$ is 0 as in amorphous materials, and the RMS is determined by multiple coulomb scattering.

2. **Channeling:** in the angular range defined by the critical angle θ_c, particles can be channeled between crystal planes. If they are trapped for the entire crystal length, they will acquire a deflection θ_b.

3. **Dechanneling:** some particles can escape from the channeled condition through elastic interactions that modify their transverse momentum, leading to intermediate deflections between 0 and θ_b.

4. **Volume reflection:** in a range defined by the geometrical characteristics of bending, volume reflection takes place, where the particles are deflected by a small constant angle.

5. **Volume capture:** some particles in the volume reflection angular range may have interactions that reduce their transverse momentum, so that they can be captured in channeling mode.

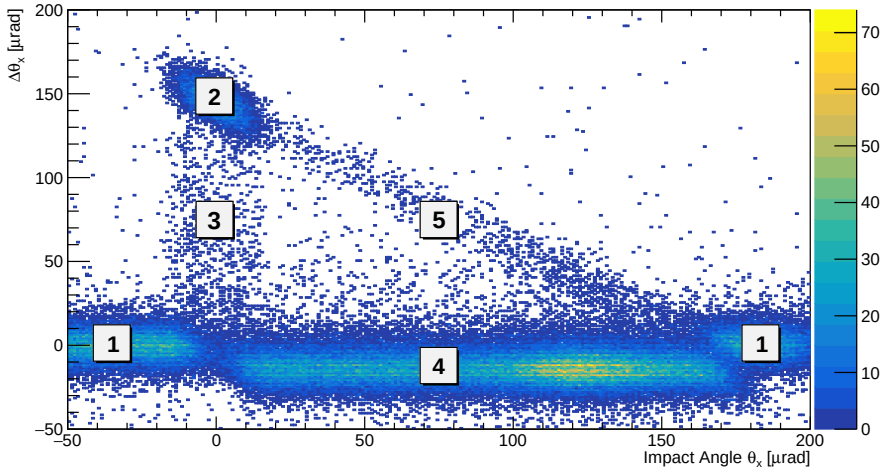

Figure 9: *Histogram resulting from an angular scan. It shows how many particles entering with an angle of $\theta_x = \theta_{in}$ are deflected by an angle of $\Delta\theta_x$. The numbers show the various processes explained in the text.*

IV. Data analysis

Collimation simulations at CERN are based on the single particle tracking code named `SixTrack` [4], which performs a symplectic six-dimensional tracking of protons through a magnetic lattice; a special version for collimation studies also models the interaction of particles with matter. When a particle interacts with a crystal a specific routine is called which uses a Monte Carlo approach based on distributions of possible interactions depending impact parameters, rather than integrating numerically their trajectory in the crystalline potential. This is necessary for the routine to be fast enough to be useful in practical applications, i.e. simulate a decent ($\sim 10^6$–10^7 for $\sim 10^2$–10^3 turns) number of particles in a reasonable amount of time. The objective of this thesis is to improve the treatment of the transition from VR->AM.

Discrepancies between the old simulations and the new data had shown the need for an improved model of the transition between volume reflection and amorphous behaviour. Referring to the marked region in **Fig. 10** and in **Fig. 11** (which show respectively the data and simulation of a case-study crystal), it can be seen that there is a clear overlapping of volume reflection and amorphous interactions in a certain angular range, that is not modeled in the simulations.

A model for this transition should be able to simulate these processes for a generic crystal. For this reason, it should depend on parameters of crystals that incorporate scaling with energy and crystal parameters.

Figure 10: *Experimental angular scan (crystal STF45). The red dashed circle shows the region of interest.*

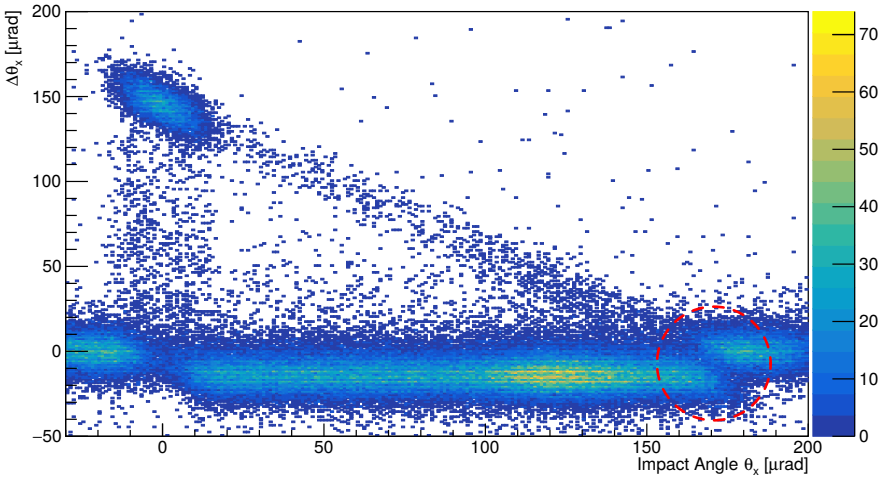

Figure 11: *Simulation of an angular scan. It is evident that the "sharp transition" is inadeguate.*

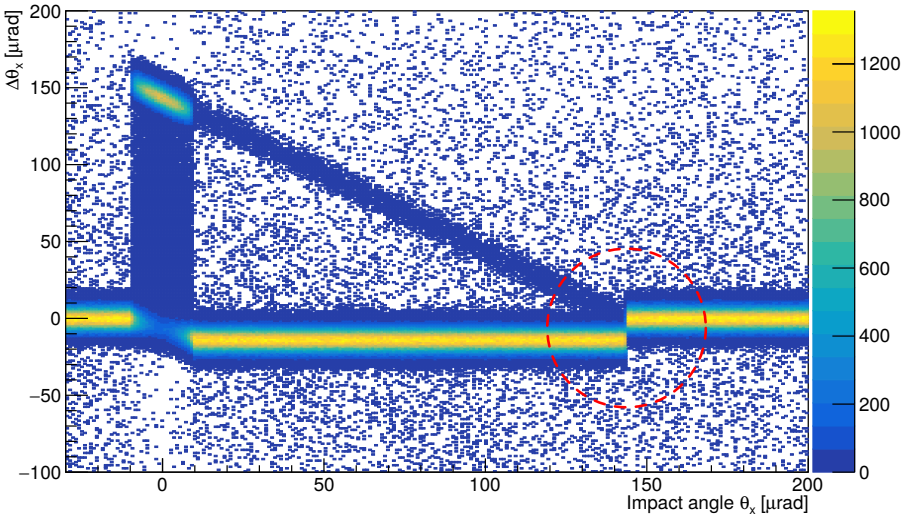

The model should, given particles with a specific θ_{in} as input, randomly distribute them according to the parametrized probabilities. Accounting for the telescope limited resolution caused by multiple coulomb scattering in the tracker planes, complicates this picture introducing *gaussian smearing*, which scatters the particles according to a gaussian distribution convoluted on top of the underlying true ones, "blurring" the histogram.

To construct the model the histogram region in question, evidenced in **Fig. 10** by the red circle, has been sliced vertically in areas of width $1\,\mu\text{rad}$, as shown in **Fig. 12**. This results in a one-dimensional distribution for each θ_{in}, that shows the number of events per $\Delta\theta$. It appears evident from **Fig. 13** that the slices have two gaussian distribution, the left one is made by the particles undergoing volume reflection, and as θ_{in} increase, it shrinks as the right one, particles undergoing amorphous scattering, increases.

To investigate the relations between θ_{in} and the particle distribution, the experimental slices obtained as described before are fitted: the most promising candidate fitting function is a simple sum of two gaussian distributions:

$$P(\Delta\theta) = C_1 e^{\frac{(\Delta\theta-\mu_1)^2}{2\sigma_1^2}} + C_2 e^{\frac{(\Delta\theta-\mu_2)^2}{2\sigma_2^2}} \tag{25}$$

Normalizing the histogram, it is clear that the particle has to be in one of the two gaussian distributions (i.e. probabilities must sum up to one), so $C_2 = 1 - C_1$ can be imposed. Moreover, as can be deducted from

their theoretical values, both σ_1, σ_2 and moreso $\Delta\sigma = \sigma_1 - \sigma_2$ are less than the overall resolution of the experimental apparatus. So especially for the slices near the edge of the region in which a peak dominate the other, to produce a more meaningful result for the important parameters (C and μ), $\sigma_1 = \sigma_2 = \sigma$ is imposed: this overall sigma/resolution can be easily derived from the dominant peak alone; the algorithm can thus improve more the remaining parameters. The resulting function thus is:

$$P(\Delta\theta) = Ce^{\frac{(\Delta\theta-\mu_1)^2}{2\sigma^2}} + (1-C)e^{\frac{(\Delta\theta-\mu_2)^2}{2\sigma^2}} \tag{26}$$

The fitting has been performed with the `scikit-learn` [5] Python machine learning framework, in particular the *gaussian mixture* package [2] has been utilized. In this package, the two means are extimated using k-means centroids, then a maximum-likelihood fit is performed on the data. Example results for some slices are shown in **Fig. 13**. The resulting weights $C = P_{\text{AM}}$ and $1 - C = P_{\text{VR}}$ for each slice are plotted in **Fig. 14**.

IV.I Error estimates with bootstrap

Since `scikit-learn` does not provide directly an error extimate of the parameters, the *bootstrapping* [3] method has been used to calculate the errors. Bootstrapping is a computationally-intensive resampling method that can be applied in a wide variety of applications such as extimating the approximate distribution and standard errors of a complicated estimator. It can be shown that bootstrap is asymptotically consistent [3] under mild[1] conditions on the underlying distribution of data.

In its simplest form, for a dataset of size N, the distribution or histogram of the data is taken and synthtetic datasets (again of size N) are repeatedly generated following the histogram as probability density distribution, using Montecarlo methods. This can be equivalently seen as *drawing with replacement* from the original dataset, to create several "new" datasets from the same data, but with the variability derived from the fact that, with replacement, every data point can appear zero times, or more than once. Then every synthtetic dataset is fitted under the same conditions as the data, so now there is a population of fitted parameters, one for each dataset. The standard error on this distribution can then be calculated: it can be shown [3] that, if the number of bootstrap iteration (and thus synthtetic datasets) is greater than $n_{\text{iter}} \approx 200$, the error deriving from Montecarlo is trascurable. Thus, the standard errors have been calculated from $n_{\text{iter}} = 500$ iterations.

[1] For example, the existence of the distribution momenta to be estimated, such as mean or standard deviation, in the underlying distribution.

Figure 12: *The slicing of the transition region into one-dimensional distributions. The 2-dimensional histogram region of* ***Fig. 10*** *is subdivided into 1-dimensional slices as indicated by the red lines. The red numbers refers to* ***Fig. 13****, where these slices are plotted and fitted.*

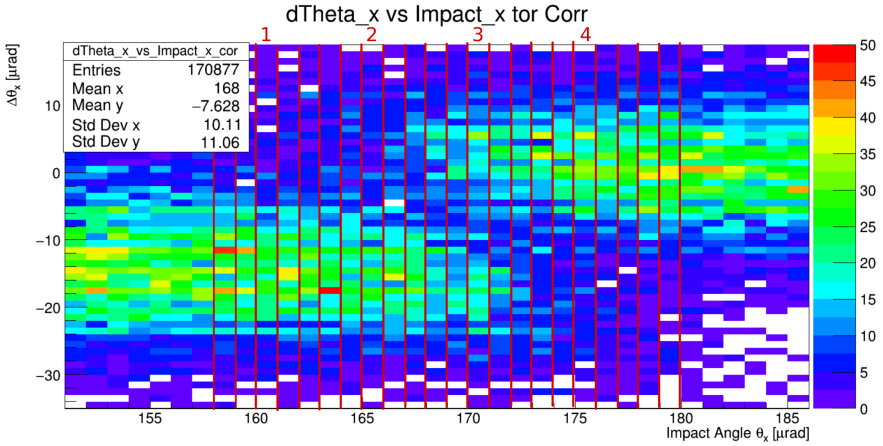

Figure 13: *Some examples of normalized slices (crystal STF45) from* ***Fig. 12*** *for increasing θ_{in}. On the abscissa $\Delta\theta$ [μrad] is shown, on the ordinate the normalized number of particles (proportion). The histogram is in blue. It is clear that there are two peaks, fitted by the green gaussians, whose sum is the red plot. Around the red plot the orange fits of the synthtetic datasets from bootstrap are plotted, used to calculate parameter errors.*

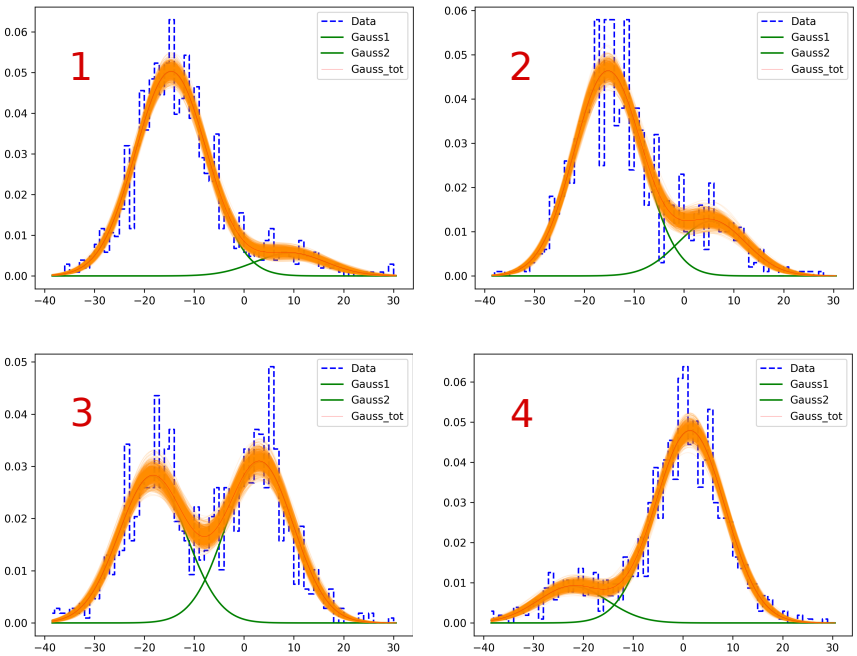

Figure 14: *The two peak probabilities or weights with their error bars, note $P_{AM} = 1 - P_{VR}$. The three vertical lines represent θ_b (green) and $\theta_b + \theta_c$, $\theta_b + 2\theta_c$ (blue).*

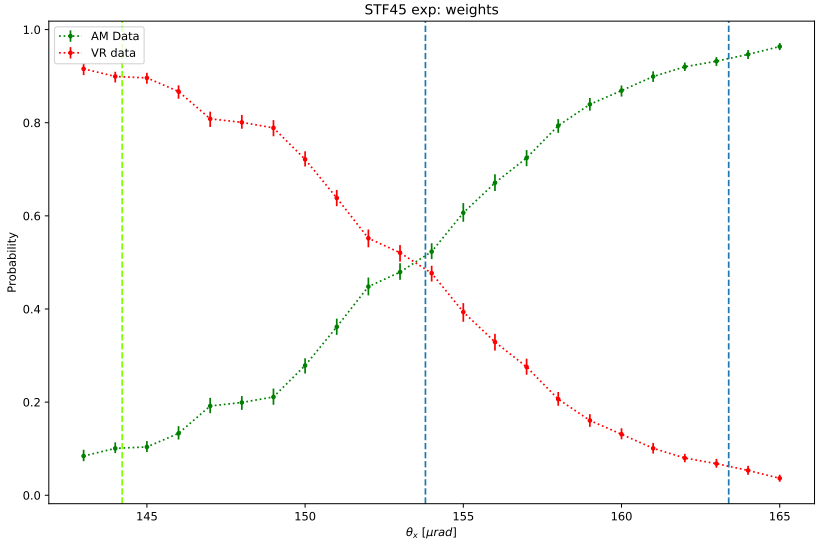

IV.II Theoretical model

The most important parameters to build a probability distribution to be used in Montecarlo simulation are the weights (the probability P of being in one or the other distribution) and the means, since for the sigmas the theoretical ones can be used. After some trials, the simple model of eq. (27) and (28) was chosen for the relative weights C and $1-C$ (plotted in **Fig. 15**):

$$C = P_{\text{AM}}(\theta_{\text{in}}) = \begin{cases} 0 & \text{if } \theta_{\text{in}} \leq \theta_b \\ \frac{-1}{2\theta_c} \cdot \theta_{\text{in}} + \frac{\theta_b}{2\theta_c} + 1 & \text{if } \theta_b < \theta_{\text{in}} \leq \theta_b + 2\theta_c \\ 1 & \text{if } \theta_{\text{in}} > \theta_b + 2\theta_c \end{cases} \tag{27}$$

$$1 - C = P_{\text{VR}}(\theta_{\text{in}}) = 1 - P_{\text{AM}}(\theta_{\text{in}}) \tag{28}$$

It was chosen as a simple transition function that satisfies the boundary conditions observed in the data. When $\theta_{\text{in}} < \theta_b$, there is only volume reflection so $P_{\text{AM}} = 0$ and $P_{\text{VR}} = 1$. On the other side, after the transition, $\theta_{\text{in}} > \theta_b + 2\theta_c$, we have only amorphous interactions, so $P_{\text{AM}} = 1$ and $P_{\text{VR}} = 0$. In the range $\theta_b \leq \theta_{\text{in}} \leq \theta_b + 2\theta_c$ there is a simple linear transition as θ_{in} increases, going from 100% volume reflection at θ_b to 0% at $\theta_b + 2\theta_c$, while the AM fraction increases corrispondently since $P_{\text{VR}}(\theta_{\text{in}}) + P_{\text{AM}}(\theta_{\text{in}}) = 1$.

For the mean deflection, eq. (29) and (30) are used (plotted in **Fig. 16**):

$$\overline{\Delta\theta_{\mathrm{AM}}}(\theta_{\mathrm{in}}) = \begin{cases} \frac{-\sigma_{\mathrm{am}}}{2\theta_c} \cdot \theta_{\mathrm{in}} + \sigma_{\mathrm{am}} + \frac{\sigma_{\mathrm{am}}\theta_{\mathrm{b}}}{2\theta_c} & \text{if } \theta_b < \theta_{\mathrm{in}} \leq \theta_b + 2\theta_c \\ 0 & \text{if } \theta_{\mathrm{in}} \leq \theta_b \end{cases} \tag{29}$$

$$\overline{\Delta\theta_{\mathrm{VR}}}(\theta_{\mathrm{in}}) = \begin{cases} \theta_{\mathrm{VR}} & \text{if } \theta_{\mathrm{in}} \leq \theta_b \\ \frac{-\sigma_{\mathrm{vr}}}{2\theta_c} \cdot \theta_{\mathrm{in}} + \theta_{\mathrm{VR}} + \frac{\sigma_{\mathrm{vr}}\theta_{\mathrm{b}}}{2\theta_c} & \text{if } \theta_b < \theta_{\mathrm{in}} \leq \theta_b + 2\theta_c \end{cases} \tag{30}$$

where σ_{AM} and σ_{VR} are the average sigma of the peaks *before* gaussian smearing. σ_{VR} can be calculated from eq. (24), while

$$\sigma_{\mathrm{AM}} = \frac{13.6\,\mathrm{MeV}}{E} Z_i \sqrt{\frac{l}{\chi_0}} \left(1 + 0.038 \log\left(\frac{l}{\chi_0}\right)\right) \tag{31}$$

is the multiple scattering angular sigma in amorphous interactions, with χ_0 being the radiation length of the material, in silicon $\chi_0(\mathrm{Si}) = 9.37\,\mathrm{cm}$.

This was derived from the observation in experimental data that the average deflection tends to drift away from the asymptotic ones (which are θ_{VR} from eq. (23), and 0 for AM) until they are about a sigma away. For VR, the average deflection $\overline{\theta_{\mathrm{VR}}}$ increases till $\overline{\theta_{\mathrm{VR}}} + \sigma_{\mathrm{VR}}$, while for AM it starts at σ_{am} and decreases to zero. So, similarly to the weights, a linear model has been created, by solving a simple system imposing a linear function $m * \theta_{\mathrm{in}} + q$ to pass through the respective limiting points for VR and AM at θ_b and $\theta_b + 2\theta_c$.

In **Fig. 17** a new simulation can be seen, to compare with **Fig. 10**. The results are in pretty good agreement with data, as explored in depth in the next section.

Figure 15: *The theoretical model for the weights. Convolution with a gaussian to account for gaussian smearing will show something close to the experimental data in **Fig. 14**.*

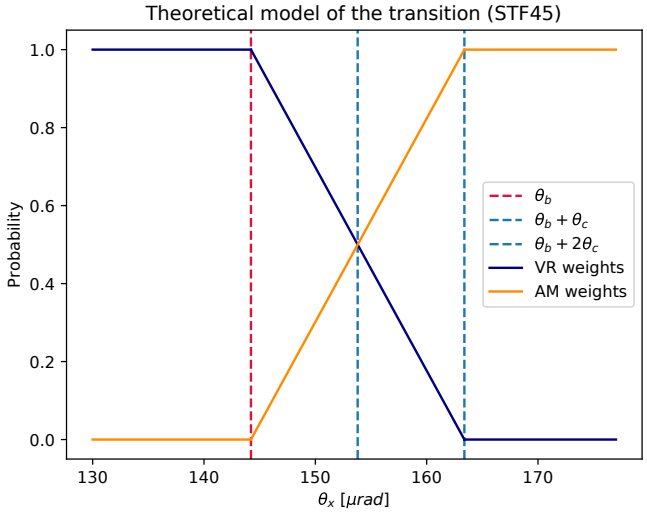

Figure 16: *The theoretical model for the means.*

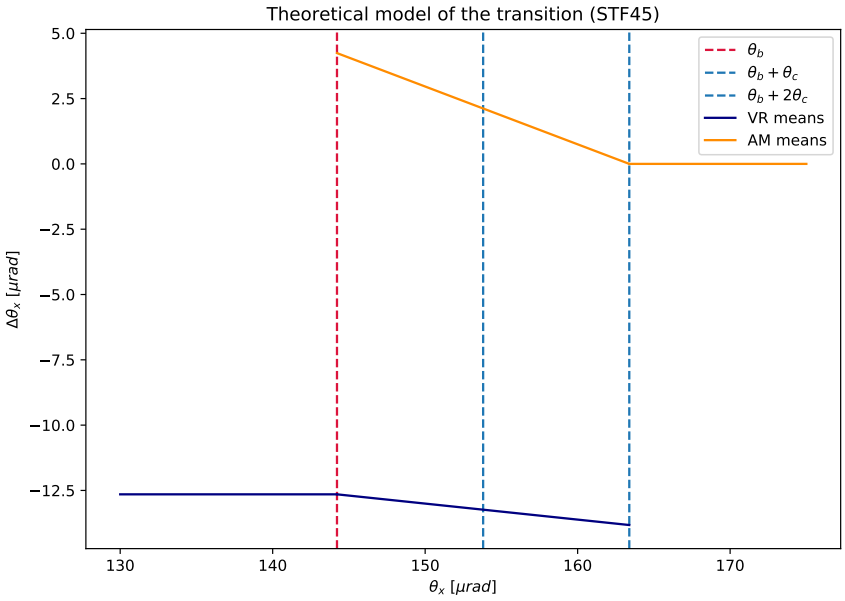

Figure 17: *Simulated angular scan (crystal STF45) with the new routine. The noise from telescope resolution has been added. This can be compared with experimental data in* ***Fig. 10****.*

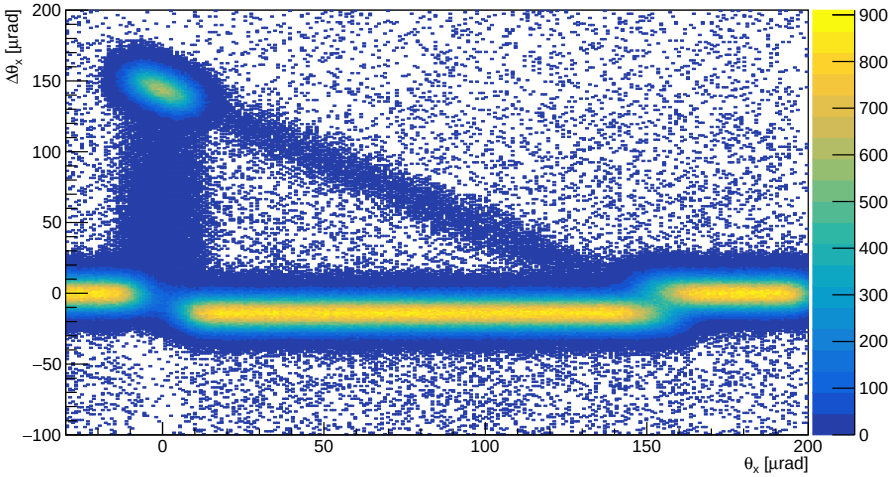

V. BENCHMARK SIMULATION RESULTS

THE SIMULATION MODEL needs to be benchmarked against experimental data. Simulations were carried out using SixTrack, even though a single passage through the crystal was simulated to reproduce tests on the H8 extraction line, described in **Sec. III**. This approach was used to avoid any problem in the migration of code from a standalone routine to the one used for simulation in circular accelerators. This benchmark validates the routine used for LHC collimation studies.

Instead of changing the crystal orientation, as in experimental angular scans, a uniform impact distribution in angle was used as input. The extention of this distribution is such that all the processes are covered. A realistic distribution in the XY plane was used, according to what was measured experimentally. This leads to easier and faster simulation results analysis, being equivalent from the physics point of view.

V.I Crystals used

Three crystals have been chosen to validate the model, because high quality angular scans were available. They are labelled as STF45, STF99 and ST101. They are crystals of the *strip* type: they have a primary curvature along the (111) planes applied through their holder, which then induces anticlastic forces resulting in a secondary curvature along the (110) planes.

Their parameters are reported in **Tab. 1**.

Table 1: *Parameters of the crystal used*

Nome	l [mm]	θ_b [μrad]	R [m]	θ_c [μrad]
STF45	2.000	144.2	13.868	9.5
STF99	1.994	122.0	16.340	9.7
ST101	1.988	162.5	12.234	9.5

V.II Benchmark

The benchmark simulations are made using the same parameters of crystals for which an angular scan is available: it can be seen in **Fig. 18**, **Fig. 19** and **Fig. 20** the comparison between experimental and simulated angular scan weights. To make a straight comparison of the simulation with the data one need to account for the resolution of the telescope, caused by multiple scattering of the particles in the tracker planes. This results in a gaussian angular scattering of the particles which "blurs" the histogram

regions. To account for this, a random gaussian kick was given to the particles, increasing the sigma until the size of the channeling spot (№ 2 in **Fig. 9**) was the same for simulation and data. This is a valid approach because the theoretical horizontal size of the channeling region, which is $2\theta_c$, is known and implemented in the simulations: it is thus possible to decouple the scattering due to the experimental apparatus.

Another potential problem, only for crystal STF45, is that the goniometer likely stopped for about $16\,\mu\mathrm{rad}$ as can be evinced from **Fig. 10** by the increased number of particles per slice after $\sim 110\,\mu\mathrm{rad}$. To correct this, the experimental slices have been shifted by $16\,\mu\mathrm{rad}$. This would influence only the model implementation of the absolute position, that is the start of the transition at θ_b, but not the independent fact that the transition has angular range width of $2\theta_c$. The absolute part is independently confirmed by the other two crystals.

After working these details out, the model benchmark can be considered successful, as the plots below shows. In **Fig. 21** and **Fig. 22** a comparison of the other parameters can be seen as well, the peak means and sigma.

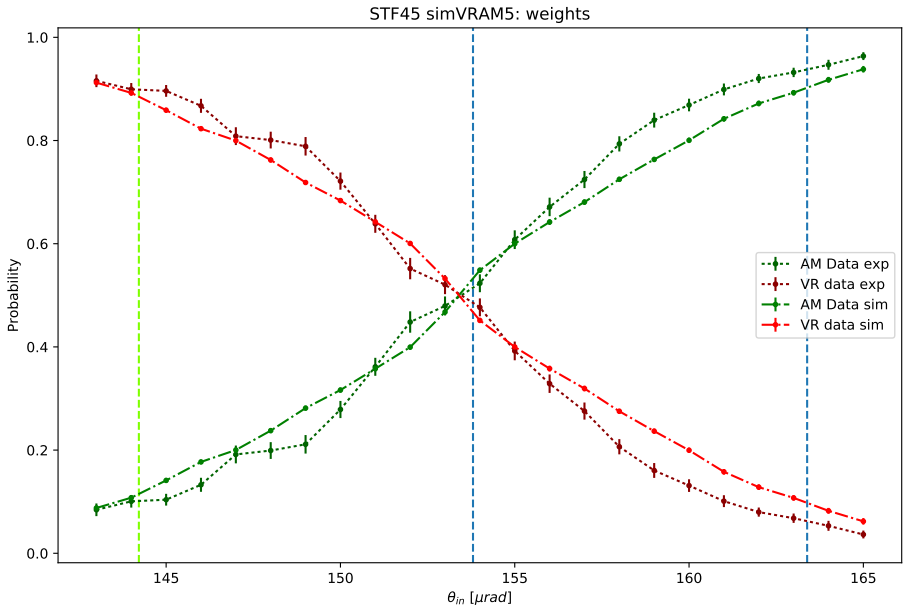

Figure 18: *Comparison of the simulation of the crystal STF45 with the experimental data: the weights or probability of a particle of being in either process as a function of the impact angle θ_x. The red lines are the weight of the volume reflection process, while the green ones are the weight of the amorphous process. The dashed lines are the fit of experimental data while the dashdot the fit of the angular scan simulation. The vertical lines are θ_b (red) and $\theta_b + \theta_c$, $\theta_b + 2\theta_c$ (blue).*

Figure 19: *Comparison of the simulation of the crystal STF99 with the experimental data: the weights: the weights or probability of a particle of being in either process as a function of the impact angle θ_x.*

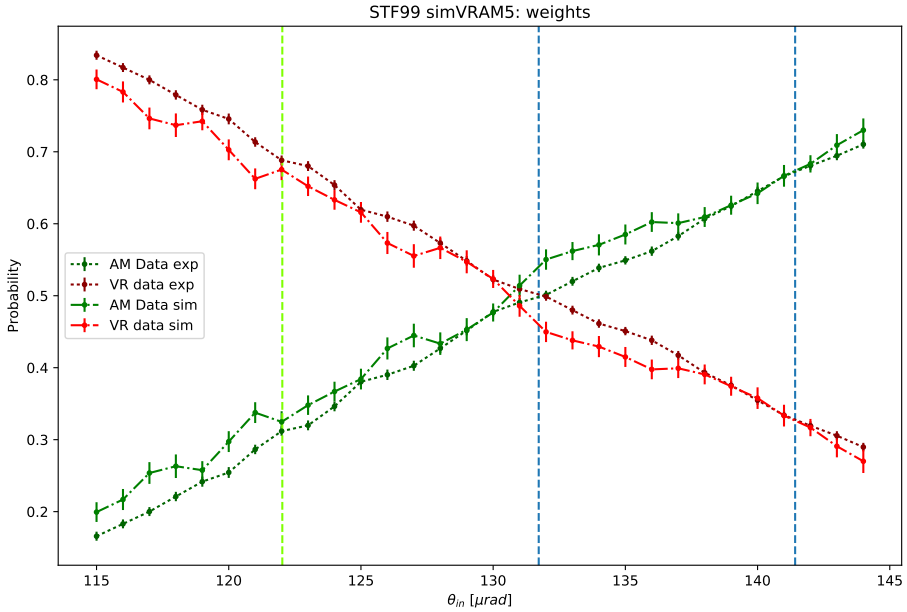

Figure 20: *Comparison of the simulation of the crystal ST101 with the experimental data: the weights or probability of a particle of being in either process as a function of the impact angle θ_x.*

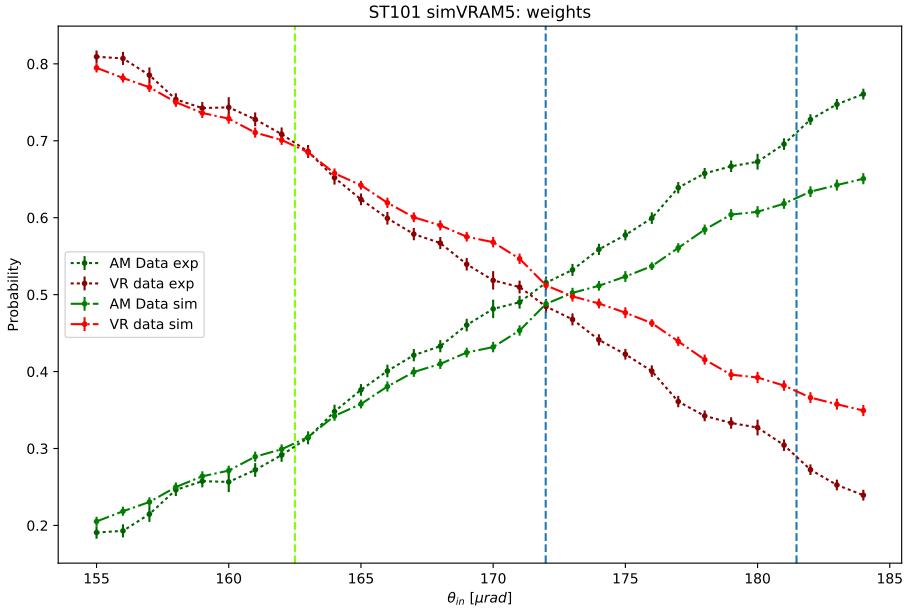

Figure 21: *Comparison of the simulation of the crystal ST101 with the experimental data: the means. The position of the mean $\overline{\Delta\theta_{AM}}$, $\overline{\Delta\theta_{VR}}$ of each peak is plotted for each slice of impact angle θ_x. The vertical lines are θ_b (red) and $\theta_b + \theta_c$, $\theta_b + 2\theta_c$ (blue), while the horizontal lines are the theoretical asymptotic values of $\overline{\Delta\theta_{AM}} = 0$ and $\overline{\Delta\theta_{VR}} = \theta_{VR}$.*

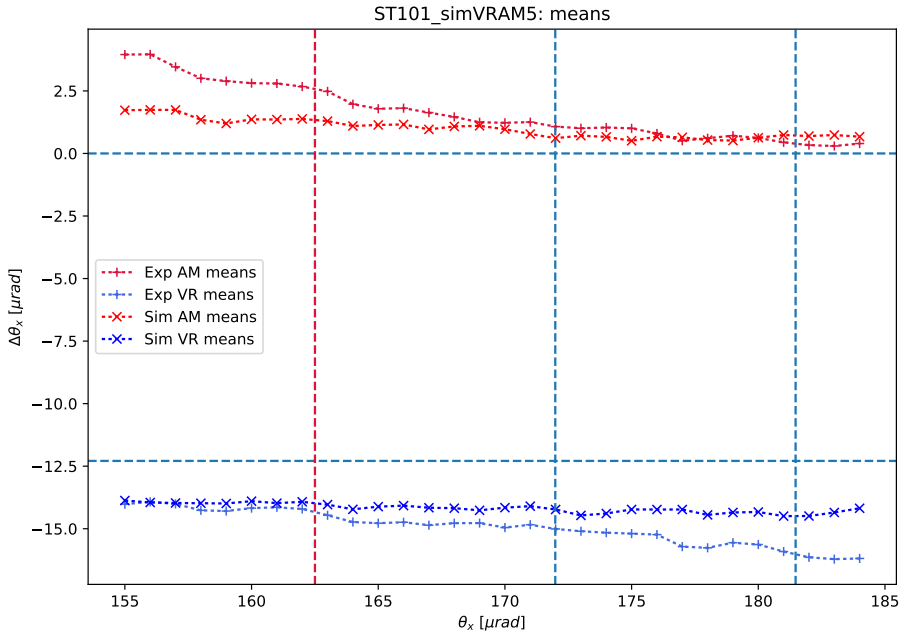

Figure 22: *Comparison of the simulation of the crystal ST101 with the experimental data: the sigma for the experimental data and for the simulation, as a function of the impact angle θ_x.*

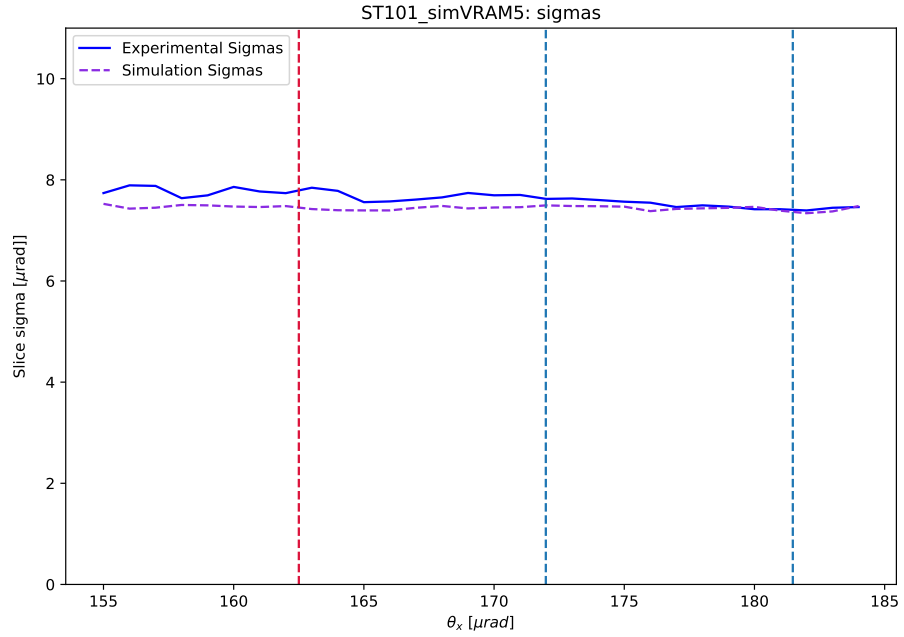

V.III Energy scaling

The energy scaling of the model has been proved using experimental data from tests at the LHC with $6.5\,\mathrm{TeV}$ proton beams.

In **Fig. 23** [7], beam loss as a function of the crystal angular orientation with respect to the beam envelope are shown. Such losses are measured using ionization chambers (BLM) that are placed near the beam pipe. BLMs measure the fraction of hadronic showers in its solid angle that are proportional to the nuclear interaction rate in upstream object.

In the two extreme shoulders the crystal behaves as an amorphous scatterer (AM). Thus losses are flat as a function of its angle. When the beginning of the crystalline planes is parallel to the beam envelope, particles are channeled (CH) between crystalline planes. In this condition they are travelling in relatively empty space between planes, and nuclear interaction rate is reduced. The plateau between CH and AM is the volume reflection (VR). The plateau between CH and AM is the volume reflection (VR). As it is known from theory, this VR range has a length of θ_b, but simulations with the old routine, shown in red in the plot, did not match the data (blue). The new routine instead, shown in green, match the observed losses much better.

This crystal is installed in the LHC and has parameters $l = 4\,\mathrm{mm}$ and $\theta_b = 50\,\mu\mathrm{rad}$. The good agreement between simulations and data shows indirectly that the scaling as a function of energy and crystal parameters of the transition model implemented in the crystal routine is adeguate.

Figure 23: *Beam loss as a function of the crystal angular orientation with respect to the beam envelope (from [7], courtesy of R. Rossi).*

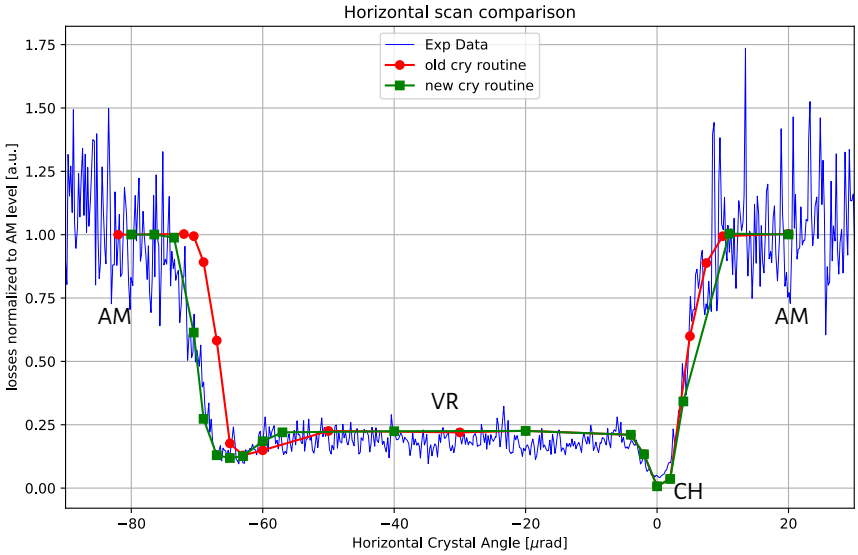

VI. CONCLUSIONS

IN THIS THESIS a new analysis of the transition region between the volume reflection and the amorphous processes has been performed. A new model is proposed based on this analysis, and simulations using the new model have been performed and benchmarked. This effect was not simulated before because the angular range of this transition is very far from the usual range used for collimation purposes, when the crystal is in channeling. Nevertheless, in preliminary studies at SPS and LHC it is necessary to look at all the interactions, and this effect is interesting because the volume reflection angular range can be used as an independent measurement of the crystal curvature.

To construct a model for the transition, the angular scan of a crystal in the extracted beam from SPS (H8 line) has been analyzed. Based on this analysis, a suitable model has been chosen. This model has been implemented (by D. Mirarchi) in the `SixTrack` routine, then the simulations have been performed and benchmarked with respect to angular scans of different crystals with different parameters.

The new routine shows a qualitatively better agreement with experimental data, although there may be room for improvements and refining of the model when new data from the latest runs will become available for analysis. Another confirmation comes from the simulation of loss maps in LHC crystals made by R. Rossi, which shows how the model scales with energy. Again, the model has improved the correspondence between loss map simulations and data.

Future developments might include benchmarking with other beam conditions such as different energies and particles, for example ions or pions.

REFERENCES

[1] Valery M. Biryukov, Yuri A. Chesnokov, and Vladilen I. Kotov. *Crystal channeling and its application at high-energy accelerators*. Springer Science & Business Media, 2013.

[2] Scikit-learn developers. *Gaussian mixture models*. 2016. URL: http://scikit-learn.org/stable/modules/mixture.html#gaussian-mixture.

[3] B. Efron and R. J. Tibshirani. *An Introduction to the Bootstrap*. CRC Press, 1994.

[4] Daniele Mirarchi. "Vol. 31-Crystal Collimation for LHC". PhD thesis. Imperial Coll., London, 2015.

[5] F. Pedregosa et al. "Scikit-learn: Machine Learning in Python". In: *Journal of Machine Learning Research* 12 (2011), pp. 2825–2830.

[6] M. Pesaresi et al. "Design and performance of a high rate, high angular resolution beam telescope used for crystal channeling studies". In: *Journal of Instrumentation* 6.04 (2011), P04006.

[7] Roberto Rossi. *Updated crystal routine — improved LHC simulation results*. 2017. URL: https://indico.cern.ch/event/623637/contributions/2516133/attachments/1442061/2220543/Rossi_ColUSM_0704_v1.00.pdf.

[8] Walter Scandale et al. "Volume reflection dependence of 400 GeV/c protons on the bent crystal curvature". In: *Physical review letters* 101.23 (2008), p. 234801.

[9] W. Scandale et al. "First results on the SPS beam collimation with bent crystals". In: *Physics Letters B* 692.2 (2010), pp. 78–82.

[10] AM Taratin and Walter Scandale. "Volume reflection of high-energy protons in short bent crystals". In: *Nuclear Instruments and Methods in Physics Research Section B: Beam Interactions with Materials and Atoms* 262.2 (2007), pp. 340–347.